Materials Science and Engineering C 42 (2014) 52–63

Contents lists available at ScienceDirect

Materials Science and Engineering C

journal homepage: www.elsevier.com/locate/msec

Effect of spatial confinement on magnetic hyperthermia via dipolar interactions in Fe_3O_4 nanoparticles for biomedical applications

M.E. Sadat [a], Ronak Patel [b], Jason Sookoor [c], Sergey L. Bud'ko [d,e], Rodney C. Ewing [f], Jiaming Zhang [f], Hong Xu [g], Yilong Wang [h], Giovanni M. Pauletti [i], David B. Mast [a], Donglu Shi [g,b,h,*]

[a] Department of Physics, University of Cincinnati, Cincinnati, OH 45221, USA
[b] The Materials Science and Engineering Program, Department of Mechanical and Materials Engineering, College of Engineering and Applied Science, University of Cincinnati, Cincinnati, OH 45221, USA
[c] Department of Neuroscience, University of Cincinnati, OH 45221, USA
[d] Ames Laboratory, Iowa State University, Ames, IA 50011, USA
[e] Department of Physics and Astronomy, Iowa State University, Ames, IA 50011, USA
[f] Department of Geological & Environmental Sciences, Stanford University, Stanford, CA 94305-2115, USA
[g] Med-X Institute, Shanghai Jiao Tong University, Shanghai 200030, PR China
[h] Shanghai East Hospital, The Institute for Biomedical Engineering & Nano Science, Tongji University School of Medicine, Shanghai 200120, China
[i] James L. Winkle College of Pharmacy, University of Cincinnati, Cincinnati, OH 45267, USA

ARTICLE INFO

Article history:
Received 23 February 2014
Accepted 26 April 2014
Available online 13 May 2014

Keywords:
Fe_3O_4 nanoparticles
Magnetic anisotropy
Dipole interaction
Superparamagnetism
Néel relaxation

ABSTRACT

In this work, the effect of nanoparticle confinement on the magnetic relaxation of iron oxide (Fe_3O_4) nanoparticles (NP) was investigated by measuring the hyperthermia heating behavior in high frequency alternating magnetic field. Three different Fe_3O_4 nanoparticle systems having distinct nanoparticle configurations were studied in terms of magnetic hyperthermia heating rate and DC magnetization. All magnetic nanoparticle (MNP) systems were constructed using equivalent ~10 nm diameter NP that were structured differently in terms of configuration, physical confinement, and interparticle spacing. The spatial confinement was achieved by embedding the Fe_3O_4 nanoparticles in the matrices of the polystyrene spheres of 100 nm, while the unconfined was the free Fe_3O_4 nanoparticles well-dispersed in the liquid via PAA surface coating. Assuming the identical core MNPs in each system, the heating behavior was analyzed in terms of particle freedom (or confinement), interparticle spacing, and magnetic coupling (or dipole–dipole interaction). DC magnetization data were correlated to the heating behavior with different material properties. Analysis of DC magnetization measurements showed deviation from classical Langevin behavior near saturation due to dipole interaction modification of the MNPs resulting in a high magnetic anisotropy. It was found that the Specific Absorption Rate (SAR) of the unconfined nanoparticle systems were significantly higher than those of confined (the MNPs embedded in the polystyrene matrix). This increase of SAR was found to be attributable to high Néel relaxation rate and hysteresis loss of the unconfined MNPs. It was also found that the dipole–dipole interactions can significantly reduce the global magnetic response of the MNPs and thereby decrease the SAR of the nanoparticle systems.

1. Introduction

In recent years, magnetic fluid hyperthermia (MFH) via superparamagnetic nanoparticles (NP) has been extensively studied for possible medical use in cancer therapy [1,2]. In MFH, superparamagnetic particles are exposed to an alternating (AC) magnetic field in which the NP oscillate with the applied field. Energy dissipation from magnetic relaxation of the magnetic nanoparticles (MNPs) generates heat and gives rise in local temperature. If the temperature of that region increases to 42–45 °C from the physiological temperature of 37 °C, the local heat generated via cell-targeted uptake in the tumor region can effectively kill cancer cells [3]. For these clinical applications, the MNPs need to maintain sufficient heating, characterized by Specific Absorption Rate (SAR), in order to destroy malignant tissues [4]. In general, SAR depends on MNPs anisotropy constant (K), saturation magnetization (M_s) particle size, and geometry [5]. The measured SAR also depends on the amplitude (H) and frequency (f) of the alternating

* Corresponding author at: College of Engineering and Applied Science, 493 Rhodes Hall, ML72, University of Cincinnati, Cincinnati, OH 45221, USA. Tel.: +1 513 556 3100.
E-mail address: donglu.shi@uc.edu (D. Shi).

http://dx.doi.org/10.1016/j.msec.2014.04.064
0928-4931/

magnetic field as well as the local properties such as the viscosity and heat capacity of the carrier liquid or surrounding tissue.

Therefore, for optimum SAR, intensive efforts have been made to investigate its dominating factors. For example, Hergt et al. reported an SAR value of 960 Wg^{-1} for a bacterial magnetosome sample measured at alternating magnetic field amplitude of 10 KA/m and a frequency of 410 KHz [6]. However, bacterial magnetosome sample is not a proper choice for biomedical applications due to the requirements of the medical reservation for bacterial protein coating [7]. The highest SAR value reported so far in literature is about 3000 W/g at alternating magnetic field of 58 KA/m and frequency of 274 KHz for metallic iron cubes with an anisotropy constant of 91 KJm^{-3} and saturation magnetization of 1700 KA/m [8]. One of the limitations of the metallic nanoparticles is inadequate biocompability in physiological environment for use in-vivo [9]. Presently, the only magnetic material with excellent biocompability and high magnetization that have been intensively used for in-vivo and in-vitro studies is the superparamagnetic iron-oxide nanoparticles [10].

In the study of magnetic hyperthermia, iron-oxide nanoparticles were found to exhibit different heating behaviors that are related to the particle size, particle geometry, inter-particle spacing, physical confinement, and surrounding environment. These are considered the key factors that strongly influence SAR. Most of the previous studies have focused on the correlations between hyperthermia heating and material characteristics such as particle size and distribution, only a few investigated effects of dipole interactions on SAR. Some earlier works indicated that magnetic dipole interactions, associated with particle surface morphologies, structures and concentrations, play an important role in hyperthermia heating behaviors [11,12]. For example Singh et al. reported an enhanced heat dissipation in an agglomerated system of 10 nm diameter superparamagnetic nanoparticles under an alternating magnetic field, due to hysteresis loss [13]. Using computer simulations they concluded that, as the number of particle/cc increases from 10^{10} to 10^{14}, a deviation from the Langevin response to the hysteresis loss is associated with the coupling of dipole–dipole interactions. However, Serantes et al. found completely opposite behavior for monodisperse single domain MNPs, in that they observed a decrease in hysteresis loss with increasing dipolar interaction which reduced the overall heating performance of the MNPs in alternating magnetic field [14].

Despite the extensive research on superparamagnetic magnetites, the fundamental hyperthermia heating mechanicals are not yet well identified, especially in terms of dipole interactions. In this study, superparamagnetic iron-oxide nanoparticles were investigated on the correlations between SAR and dipole interactions. A systematic study was carried out using four different superparamagnetic Fe_3O_4 nanoparticle systems with different structural and magnetic properties. The first system consists of the as-synthesized, uncoated Fe_3O_4 nanoparticles, with an average diameter of 9 nm, (denoted as Uncoated/Fe_3O_4). The second system is the Fe_3O_4 nanoparticles coated with polyacrylic acid (PAA) (denoted as PAA/Fe_3O_4). The third is the polystyrene nanosphere (NS) with 10 nm diameter Fe_3O_4 nanoparticles uniformly embedded in its matrix, which has an overall average diameter of 100 nm (denoted as PS/Fe_3O_4). The last system, which is the same as PS/Fe_3O_4 but with silica thin film surface coating (denoted as Si/PS/Fe_3O_4). As these nanoparticle systems are structurally and characteristically different in terms of particle size, surface functionalization, physical confinement, and interparticle spacing, the magnetic and hyperthermia behaviors are altered. With these variables, the operating mechanism on hyperthermia heating was identified with a dipole–dipole interaction model. A relationship was established between the physical configuration of nanoparticles and heating behaviors. The magnetic hyperthermia heating was attributed mainly to Néel relaxation and hysteresis loss. Magnetic hyperthermia heating by Néel relaxation was found to be affected by dipole–dipole interactions for the nanoparticle systems. A physical dipolar interaction model was proposed to interpret the hyperthermia heating behaviors of all nanoparticle systems.

2. Experimental details

Uncoated Fe_3O_4 nanoparticles were synthesized using a co-precipitation method, where 2.00 g (0.01 mol) of $FeCl_2 \cdot 4H_2O$ and 5.5 g (0.02 mol) of $FeCl_3 \cdot 6H_2O$ (Sigma-Aldrich, St. Louis, MO, USA) were first dissolved in 50 mL distilled H_20 at 80 °C in a nitrogen environment. While continuously stirring this mixture, aqueous sodium hydroxide (NaOH) was slowly added to precipitate Fe_3O_4 particles. After the mixture was then stirred at 80 °C for another 3 h in a nitrogen environment Fe_3O_4 nanoparticles were magnetically separated from the solution and then washed repeatedly with distilled water to remove any unprecipitated iron salts from the solution.

The procedure for synthesizing PAA/Fe_3O_4 and NS samples are described in our previous report, where PAA coated single Fe_3O_4 nanoparticles were prepared using polyol method [15]. Fe_3O_4 nanoparticles that were encapsulated in the polystyrene nanospheres were first synthesized via a co-precipitation method [16], which combined a modified miniemulsion/emulsion polymerization and sol–gel technique. Some of the PS/Fe_3O_4 composite nanospheres (NS) were further functionalized to give a surface layer of silica i.e. coating the entire PS/Fe_3O_4 NS [17]. Finally, all the nanoparticle samples were dispersed in H_2O.

X-ray diffraction (XRD) measurements were carried out for characterization of the nanoparticle samples. The nanoparticle solution was first dried onto a glass substrate and X-ray diffraction pattern was recorded on a Siemens D-500 X-ray diffractometer using a CuKα (1.5406 A°) radiation source. All the samples were scanned in the 2θ range of 5° to 65° at a step size of 0.01°.

Transmission electron microscopy (TEM) images were taken using a JEOL 2010F to study the morphology of MNPs. Samples were prepared for TEM by putting a drop of MNP solution on a carbon coated copper grid and letting it dry at room temperature. The mean hydrodynamic diameter and size distribution of the MNPs dispersed in water were measured by Zetasizer Nano Series, Malvern Instruments.

Thermogravimetric analysis (TGA) of each type of MNP samples was carried out using a TGA (Model-Q 50) at room temperature to 700 °C at a temperature scan rate of 20 °C/min in N_2 atmosphere.

DC magnetization data were obtained at temperature T = 300 K using a Quantum Design MPMS-5 superconducting quantum interference device (SQUID) up to a maximum field amplitude of ± 10 kOe.

The magnetothermal properties of the MNP systems were characterized using a home-made magnetic hyperthermia system (shown in Fig. 1). The system consists of the magnetic field generation system, temperature monitoring, and a water circulation system to prevent heat from the coil affecting the samples. The 10 turn coil used in this work is 84 mm long and has an inner diameter of 39 mm, and is made of 1/8″ copper tubing. The coil is wound around a hollow G-10 cylinder with two 1/8″ thick rectangular G-10 pieces attached on both ends of the G-10 cylinder for support. The inner volume of the cylinder is filled with styrofoam insulation except for an open center volume for the insertion of the sample vial into magnetic field region. The magnetic field is produced using a sinusoidal 13.56 MHz AC signal, generated by a ENI OEM-6 radio frequency generator, with a maximum output of 750 W. The AC signal is applied to the copper coil circuit through a matching network. The matching network consists of a tuning box (MFJ Versa Tuner V) and a separate high-voltage variable capacitor (capacitance ranges from 10 pF to 80 pF) connected in series with the coil. The inductor selector and π section capacitor in the tuning box are varied until maximum (minimum) forward (reverse) signal is observed. In this way, a resonance condition is established when the impedance of the load matches the power amplifier. A 2 mm outer diameter pick up coil made of two turns of AWG 30 copper wire was used to determine the strength of the magnetic field created in the coil. The magneto thermal heating measurements were carried out using a glass vial containing 1 mL of magnetic nanoparticle solution placed at the center of the copper coil. All the temperature measurements were made using a FISO

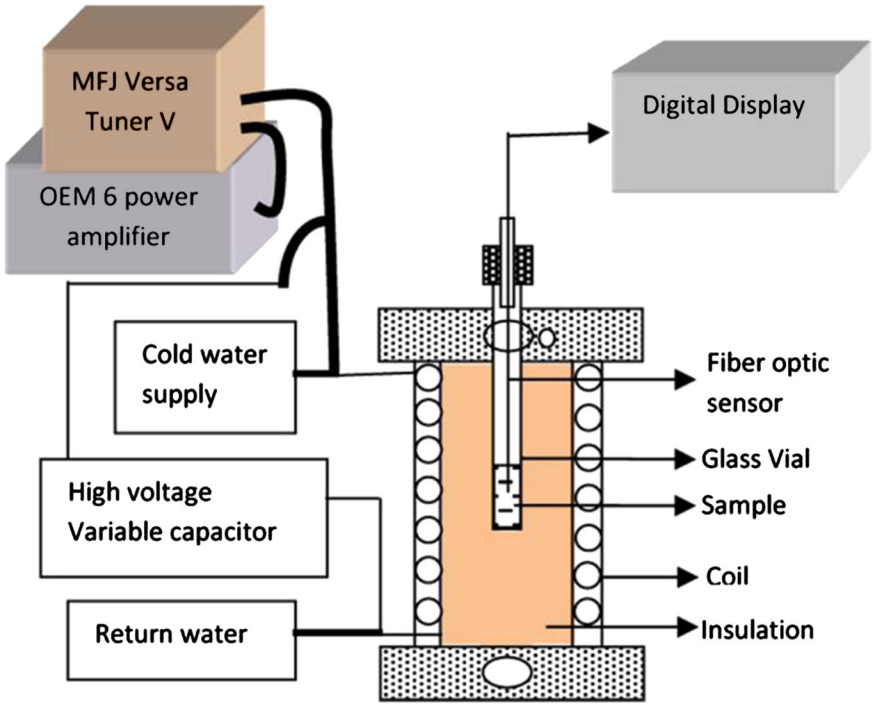

Fig. 1. Schematic of experimental set up of the magnetic hyperthermia system (MHS).

fiber optic temperature sensor (FOT-L-SD) attached to a signal conditioner (FTI-10). During the magnetothermal measurements, room temperature tap water was continuously passed through the copper tubing in order to remove the heat generated from the coil by the high AC current.

3. Results and discussion

3.1. X ray diffraction (XRD)

All 2θ scan diffraction peaks of each nanoparticle system were analyzed and found to match those of magnetite from the database code amcsd 0002404. The analysis of the diffraction pattern in Fig. 2(a) shows that the diffraction peaks of the Fe_3O_4 nanoparticles correspond to (220), (311), (400), (511), and (440) planes which indicate an inverse spinel type of structure [18]. Using the diffraction angle of the (311) peak the lattice constant (a) is calculated to be 8.3122 A , which is comparable to the lattice constant a = 8.394 A of the bulk magnetite reported in JCPDS card No 790417. However, the calculated lattice constant is also found to be a close match with the γ-Fe_2O_3 indicating that the composition of the particles is in between Fe_3O_4 and γ-Fe_2O_3. Broadening of the XRD peaks can be attributed to the particle size of powdered samples. There are several mathematical approaches such as the Variance method [19], the Scherer method [20], and the Bertaut–Warren–Averbach (BWA) method [21], by which the crystal size of the nanoparticles can be determined from the increased width and reduced height of the diffraction peaks. The Variance method provides information related to the mean size, while the Scherer method gives the mean crystallite thickness. The BWA method however can be used to calculate the mean crystalline size, strain and size distribution of the particles.

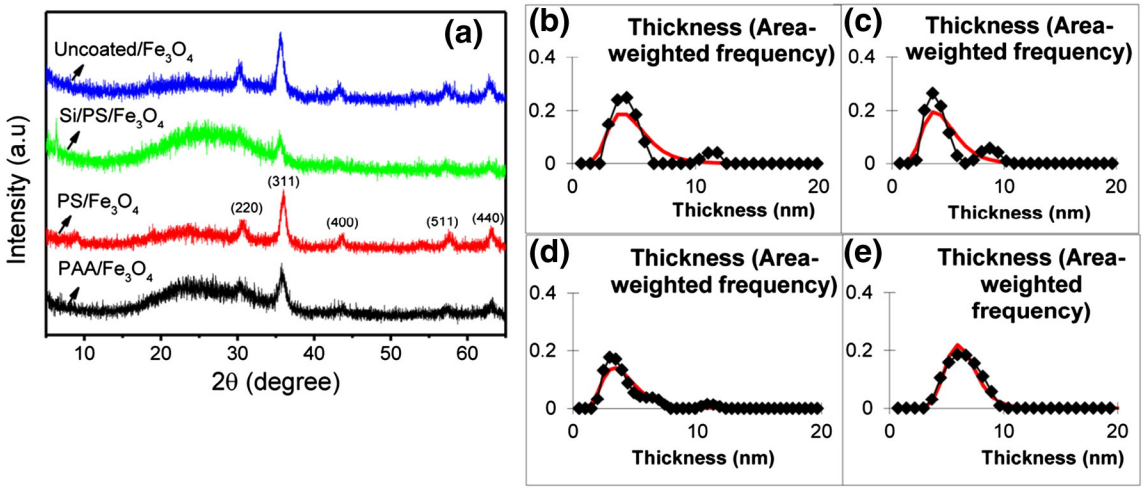

Fig. 2. (a) X-ray diffraction results of as synthesized Fe_3O_4 nanoparticles. Area weighted thickness distribution of (b) Uncoated/Fe_3O_4 (c) PAA/Fe_3O_4 (d) PS/Fe_3O_4 and (e) Si/PS/Fe_3O_4 nanoparticles calculated by Mudmaster program and solid line (red) is the corresponding lognormal distribution fitting. (For interpretation of the references to color in this figure legend, the reader is referred to the web version of this article.)

This method employs an excel based program known as Mudmaster, which was created by Drits et al. [22]. In the present study, the Mudmaster program was used to calculate the mean crystallite dimensions and distribution of diameters of the Fe_3O_4 nanoparticles. The information regarding the mean crystallite size and distributions can be calculated from the interference function (ϕ). The interference function (ϕ) is related to the intensity (I) of the diffraction pattern by the following relationship [22]:

$$I(2\theta) = Lp(2\theta)G^2(2\theta)\phi(2\theta) + b_g \quad (1)$$

where Lp is the Lorentz polarization function, G is the structure factor, and b_g is the background. The Mudmaster programs automatically correct the Lp, G, and b_g before interference function (ϕ) is submitted for the Fourier analysis. Therefore, the resulting analysis for ϕ is precise as shown by Drits et al. and Eberl et al. [23]. In the present study, the crystallite size and size distribution are calculated from the (311) peak which shows the strongest reflection. Fig. 2(b–e) shows the area weighted thickness distribution of various Fe_3O_4 nanoparticle samples as determined by the BWA technique. Table 1 shows the mean area weighted thickness distribution, mean crystallize size determined from extrapolated mean, and volume weighted thickness distribution calculated using the Mudmaster program of different samples used in this study.

3.2. Transmission electron microscopy (TEM) and Dynamic Light Scattering (DLS)

Fig. 3(a–d) shows the transmission electron microscopy (TEM) images of Uncoated/Fe_3O_4, PAA/Fe_3O_4, PS/Fe_3O_4, and Si/PS/Fe_3O_4 samples, respectively. Fig. 3(a) and (b) shows that the mean size of Fe_3O_4 in the Uncoated/Fe_3O_4 and PAA/Fe_3O_4 is 9 nm in diameter. Fig. 3(c) shows that the Fe_3O_4 nanoparticles are approximately 10 nm diameter and are embedded in the spherical polystyrene matrix having an overall mean diameter of 100 nm. PS/Fe_3O_4 with a thin silica surface coating (Si/PS/Fe_3O_4) shown in Fig. 3(d) has nearly identical Fe_3O_4 sizes and distributions. As can be seen from these figures, none of the individual Fe_3O_4 NP in each material was monodispersed. According to a report by Dormann et al., the size distribution of the particles for non-uniform distribution of nanoparticles can be well described by the lognormal function of the form [24]:

$$f(d) = \frac{1}{\sqrt{2\pi}\sigma d}\exp\left[\frac{-\ln^2\frac{d}{d_c}}{2\sigma^2}\right] \quad (2)$$

where d_c is the mean particle diameter and σ is the standard deviation. The size distribution of each system was calculated and the corresponding histogram, with the associated log normal fit is shown as an inset of Fig. 3(a–d). From the fit it was found that, the mean sizes of the particles in Uncoated/Fe_3O_4, PAA/Fe_3O_4, PS/Fe_3O_4 and Si/PS/Fe_3O_4 are 8.82 ± 0.175 nm, 8.96 ± 0.77 nm, 215.78 ± 55.51 nm and 118.57 ± 6.14 nm respectively.

Table 1
Thickness distribution of MNPs calculated by Mudmaster program.

Sample information	Thickness (area weighted) (nm)	Extrapolated mean (nm)	Thickness (volume weighted) (nm)
Uncoated/Fe_3O_4	3.4	4.9	5.9
PAA/Fe_3O_4	3.6	4.2	5.1
PS/Fe_3O_4	4.6	4.7	5.5
Si/PS/Fe_3O_4	5.6	6.4	6.7

Fig. 4(a–d) shows the hydrodynamic size determined by DLS, the mean diameters of Uncoated/Fe_3O_4, PAA/Fe_3O_4, PS/Fe_3O_4, and Si/PS/Fe_3O_4 nanoparticle samples are 295 nm, 32 nm 227 nm, and 191 nm, respectively. The polydispersity index (PDI) is a measure of aggregation in the sample. The PDI, determined by the Zeta Sizer DLS system, for the Uncoated/Fe_3O_4, PAA/Fe_3O_4, PS/Fe_3O_4 and Si/PS/Fe_3O_4 samples was found to be 0.333, 0.132, 0.183 and 0.143 respectively. The relatively high polydispersity index of Uncoated/Fe_3O_4 indicates considerable agglomeration in this system. The DLS measurements of these nanoparticle systems at higher concentrations exhibit increased hydrodynamic sizes (not shown), which indicate progressed particle aggregation at higher concentrations. This result is consistent with one of our recent observations [25].

3.3. Thermogravimetric analysis

Thermogravimetric analysis (TGA) of each sample was carried out on 1 mL of the 10 mg/mL magnetic nanoparticle solution that was dried at 46 °C for over 24 h. A portion of the sample was transferred to the TGA balance for the measurement. Fig. 5 shows the TGA analysis curves of different Fe_3O_4 samples. In each of the curves, a weight loss of 1–2 wt.% occurs below 200 °C corresponding to evaporation of moisture. For Uncoated/Fe_3O_4, a weight loss of 15% occurs from 90 °C and continues up to 280 °C, which is possibly due to evaporation of water and organic components from the surface of the aggregated nanoparticles. PAA/Fe_3O_4 exhibits two weight loss steps at around 230 °C and 430 °C. The first weight loss (3%) at 230 °C can be attributed to evaporation of moisture and the second one (10%) at 430 °C to the decomposition of PAA on the surface of the Fe_3O_4 nanoparticles. As the temperature increases further a continuous decrease in weight loss can be seen from the TGA data of PAA/Fe_3O_4. This analysis also confirms that the PAA coating was formed on the surface of the Fe_3O_4 nanoparticles. For the polystyrene/Fe_3O_4 nanosphere sample, a rapid decrease in weight loss (20%) is observed at 430 °C, which is associated with the burn out of polystyrene at that specific temperature. This result is consistent with the thermogravimetric analysis performed by Xu et al. for the same Polystyrene/Fe_3O_4 nanosphere system [17]. However, thermogravimetric analysis of Si/PS/Fe_3O_4 sample does not exhibit any significant weight loss, which is possibly due to high melting point of silica about 1600 °C. This analysis confirms the silica shell on the surface of the PS/Fe_3O_4 nanosphere, which indeed gives a good stability of this nanoparticle for biomedical applications.

3.4. Magnetic property measurements

Fig. 6(a–d) shows the magnetization curves of Uncoated/Fe_3O_4, PAA/Fe_3O_4, PS/Fe_3O_4, and Si/PS/Fe_3O_4, respectively, at different Fe_3O_4 concentrations. All curves exhibit reversible hysteresis curve with almost zero retentivity and coercivity, showing the superparamagnetic nature of these samples. As can be seen from the figures, the saturation magnetization increases with increasing Fe_3O_4 concentration for all samples. This behavior indicates that the superparamagnetic nanoparticles are non-interacting at high field. For a non-interacting system, the magnetization (M) of a dilute assembly of superparamagnetic particles in an external magnetic field (H) can be well described by the Langevin function [26]:

$$M = M_s L(x) = M_s\left(\coth(x) - \frac{1}{x}\right) \quad (3)$$

where M_s is the saturation magnetization, $x = \frac{\mu_o mH}{k_b T}$, m being the magnetic moment, μ_o is the permeability of free space, k_b is the Boltzmann constant, and T is the absolute temperature. The magnetic moment (m) can be extracted by fitting Eq. (3) with experimental magnetization curve.

Assuming at a high field magnetization is unaffected by any interaction, experimental magnetization data of each sample is fitted [Fig. 7(a–

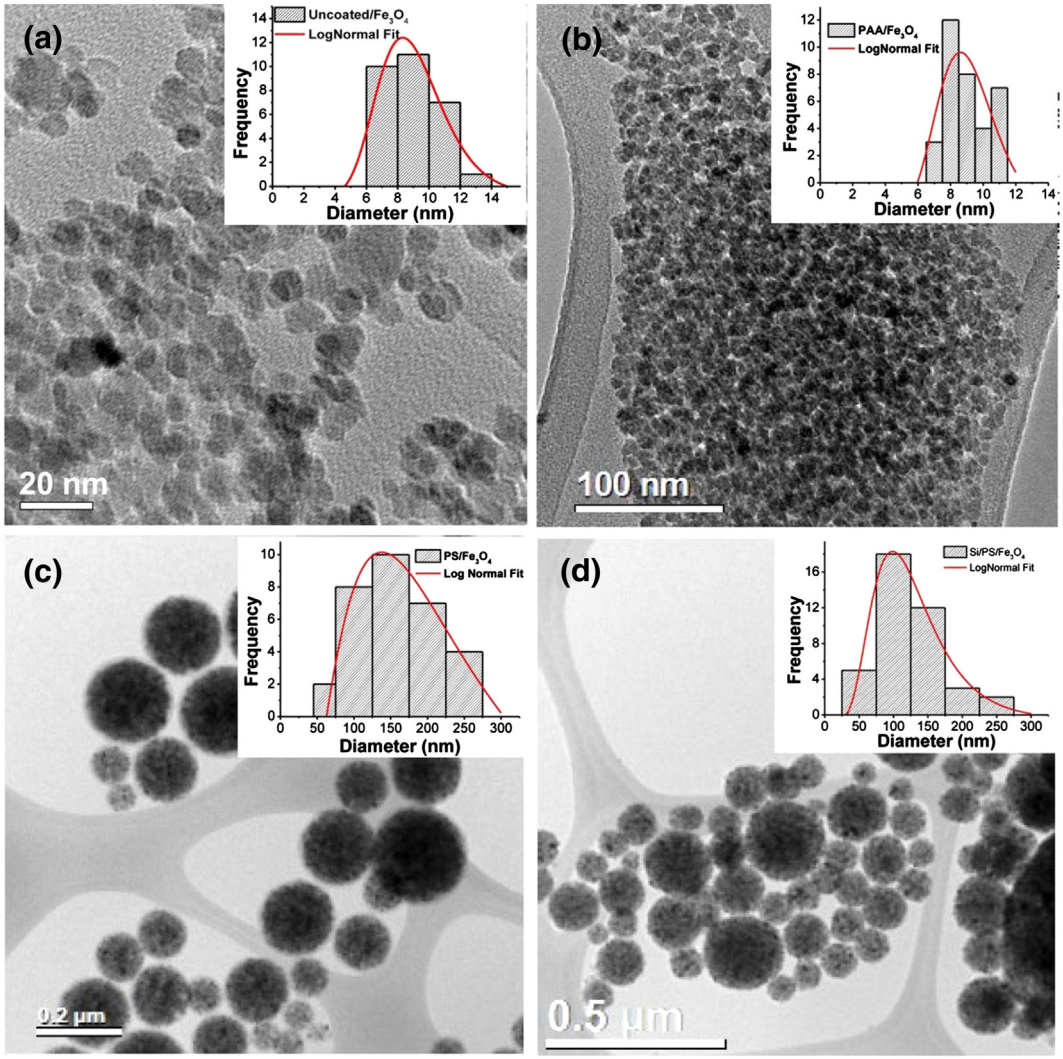

Fig. 3. Transmission electron microscopy image of (a) Uncoated/Fe_3O_4 (b) PAA/Fe_3O_4 (c) PS/Fe_3O_4 and (d) Si/PS/Fe_3O_4 nanocomposites and inset shows the corresponding histogram with log normal fitting.

d)] by Eq. (3). From fitting, the obtained values of the magnetic moments of the individual MNPs are $m = 2.72 \times 10^{-19}$ Am^2 for Uncoated/Fe_3O_4, $m = 6.35 \times 10^{-19}$ Am^2 for PAA/Fe_3O_4, $m = 2.35 \times 10^{-19}$ Am^2 for PS/Fe_3O_4, and $m = 2.45 \times 10^{-19}$ Am^2 for Si/PS/Fe_3O_4. A discrepancy between the experimental and theoretical curves for each sample can be seen near saturation, which can be attributed to the magnetic anisotropy being present in the Fe_3O_4 nanocrystals. However, non-magnetic surfactant layer does not have any contribution to magnetization and

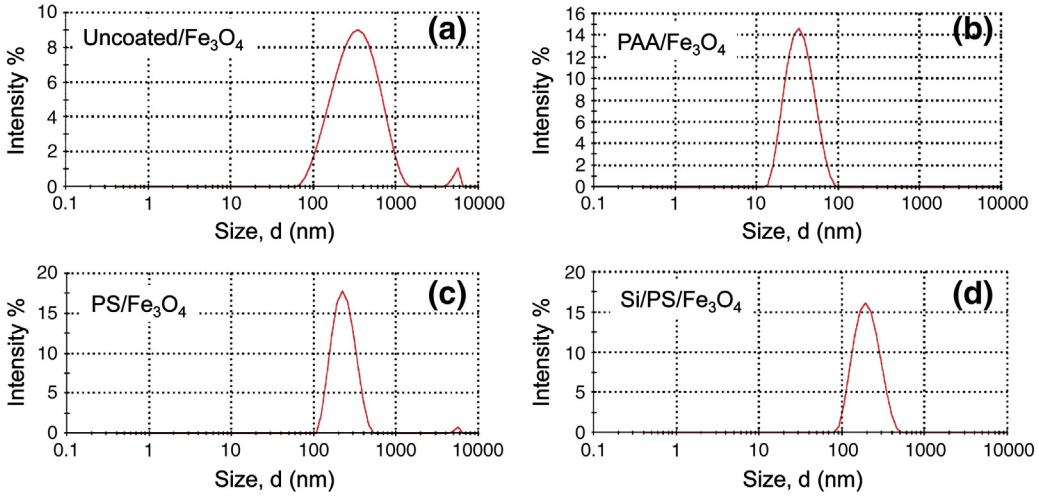

Fig. 4. Hydrodynamic size distribution of (a) Uncoated/Fe_3O_4 (b) PAA/Fe_3O_4 (c) PS/Fe_3O_4 and (d) Si/PS/Fe_3O_4 nanocomposites.

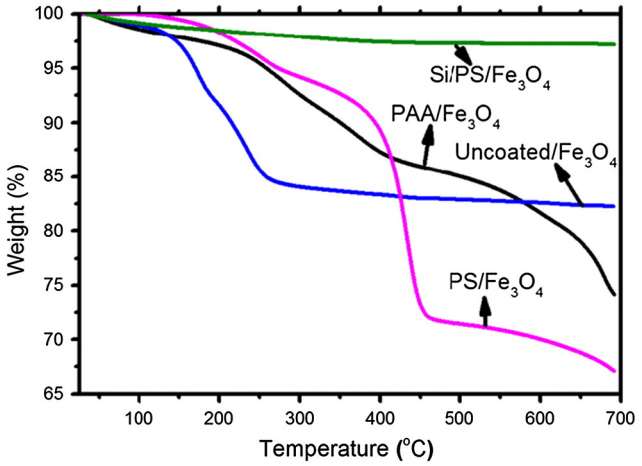

Fig. 5. Thermogravimetric analysis (TGA) results of different Fe_3O_4 nanocomposite systems.

resulting response in the applied magnetic field is coming from the magnetic materials. Therefore each sample is rescaled for magnetization per unit mass of the Fe_3O_4 nanoparticles using the TGA results. Consequently, the saturation magnetization of 293 KA/m, 325 KA/m, 321 KA/m, 309 KA/m is obtained for Uncoated/Fe_3O_4, PAA/Fe_3O_4, PS/Fe_3O_4 and Si/PS/Fe_3O_4 respectively. Fig. 8 shows the magnetization per gram of Fe_3O_4 nanoparticles for each sample.

The classical Langevin equation is derived considering the fact that the MNPs are isotropic. But in reality, such a condition is not well satisfied when different magnetic anisotropies are present in the nanocrystals [27]. The magnetic anisotropy energy of particles in an external magnetic field is given by [28]:

$$\frac{E(\theta,\varphi)}{k_bT} = \sigma_{\sin^2}\theta - \xi\cos(\theta-\varphi), \tag{4}$$

where, $\sigma = \frac{K_{eff}V}{k_BT}$ and $\xi = \frac{\mu_o M_s VH}{k_BT}$, K_{eff} is the effective anisotropy constant, V is the volume of the particle, θ is the angle between the anisotropy axis and magnetization, and φ is the angle between the applied magnetic field and the anisotropy axis. Using the thermal equilibrium function derived by Respaud et al., the magnetization (M) of the particle can be numerically calculated using the following equation [29,30]:

$$M = \int_0^{\pi/2} M(\varphi)\sin(\varphi)d\varphi. \tag{5}$$

Respaud et al.'s numerical calculations showed that for values of σ less than 1–2, there was no effect on the calculated magnetization due to magnetic anisotropy. As the anisotropy constant increases, deviation from the Langevin equation becomes significant but low field magnetization is still unaffected by magnetic anisotropy. Under this condition, magnetic anisotropy of the nanoparticles can be approximated from the experimental high field magnetization using a modified relationship for magnetic saturation. At sufficiently high field (H), magnetization of the particles can be calculated by the following equation [31]:

$$M = M_s\left(1-\frac{b}{H^2}\right), \tag{6}$$

where M_s is the saturation magnetization and b is a constant associated with the magnetocrystalline anisotropy. For large fields, plots of experimental values of M vs $1/H^2$ should give a straight line with the value of b determined from the slope and the saturation magnetization from the intercept at $1/H = 0$. For a uniaxial magnetic nanocrystal, the effective anisotropy of the particle can be approximated by the equation: $K_{eff} = \mu_o M_s\left(\frac{15b}{4}\right)^{1/2}$ (see supplementary information of ref. 4), whenever the value of b is known. Using this relationship, the effective anisotropy constant of 106.24 KJm^{-3}, 56.92 KJm^{-3}, 87.82 KJm^{-3},

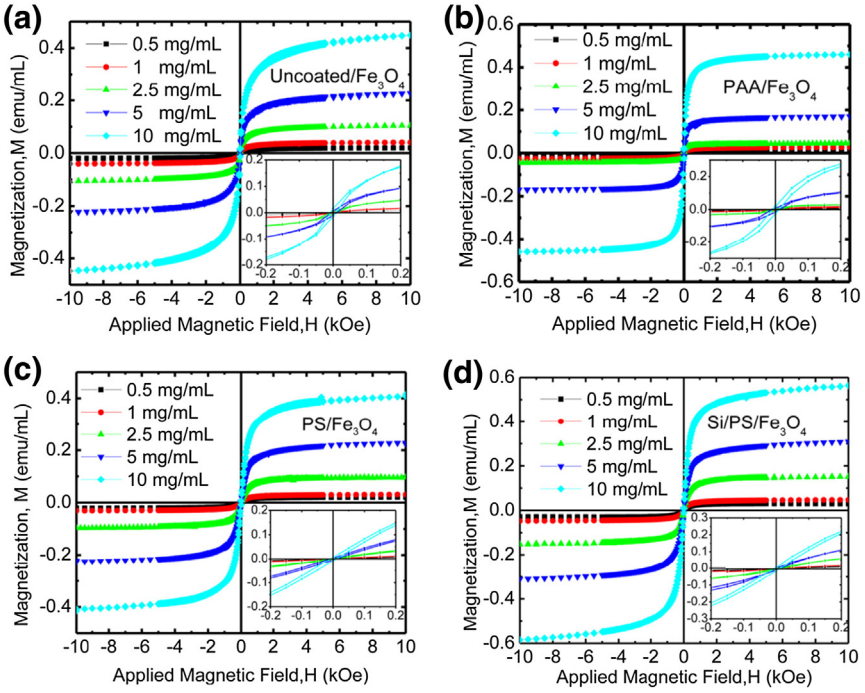

Fig. 6. DC magnetization curve from SQUID system for (a) Uncoated/Fe_3O_4 (b) PAA/Fe_3O_4 (c) PS/Fe_3O_4 and (d) Si/PS/Fe_3O_4 nanocomposite systems at different concentrations and inset shows the magnetization curve at a very low field.

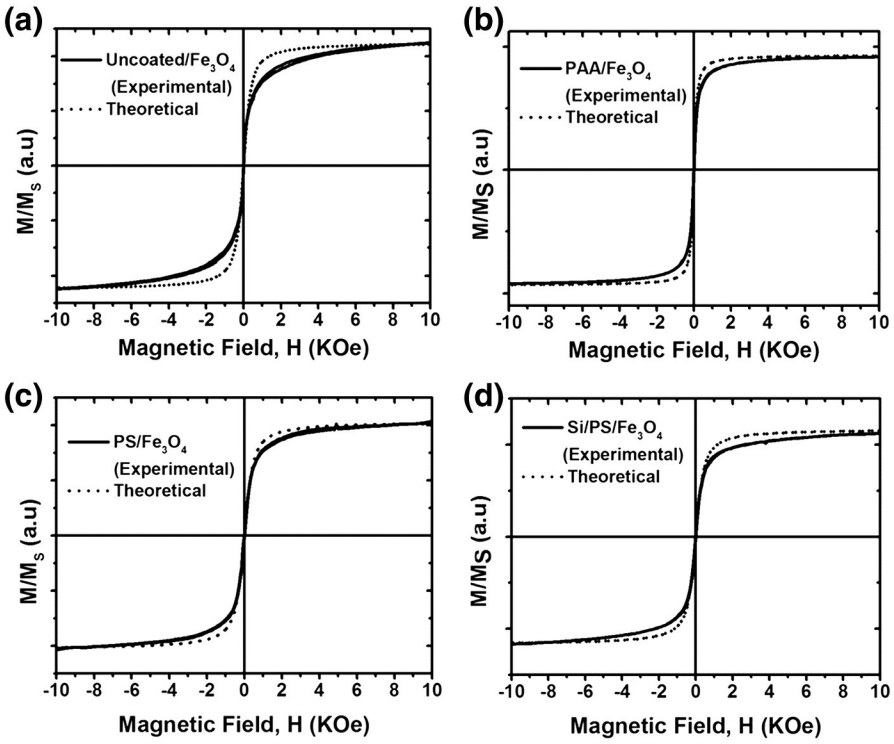

Fig. 7. Solid line represents experimental magnetization curve of different samples and dotted line represents the theoretical fitting of Langevin expression.

100.26 KJm^{-3} is obtained for Uncoated/Fe_3O_4, PAA/Fe_3O_4, PS/Fe_3O_4, and Si/PS/Fe_3O_4 respectively. The corresponding values of σ are 9.7, 5.1, 8.0 and 9.2 for Uncoated/Fe_3O_4, PAA/Fe_3O_4, PS/Fe_3O_4 and Si/PS/Fe_3O_4 respectively, which is well above the Langevin limit of 1–2. Therefore, these nanoparticle systems are in the moderately high anisotropic region as described by Respaud et al.

3.5. Magneto thermal property

The heating behaviors of different nanoparticle systems were measured at total mass concentrations of 0.5, 1, 2.5, 5, and 10 mg/mL. A 1 mL of sample of each concentration was exposed to a 13.56 MHz alternating magnetic field with amplitude of 4500 A/m. All samples were exposed to the same magnetic field for 35 min and temperature measurements were performed at a 2 minute interval using a FISO optical fiber temperature probe. Fig. 9(a) and (b) shows the time dependent temperature curves of Uncoated/Fe_3O_4 and PAA/Fe_3O_4 at various nanoparticle concentrations. The temperature of the sample reaches a saturation temperature after a period of time, as the heat generation is balanced by the heat loss of the nanoparticle system. It can be seen from the figure that the saturation temperature depends on the particle concentration of the liquid solution, with higher saturation temperature observed for higher volume fractions of Fe_3O_4. Fig. 9(c) shows the time dependent temperature curve of each MNP sample at a fixed concentration of 10 mg/mL. As can be seen from the figure, for 10 mg/mL magnetic nanoparticle solution the PAA/Fe_3O_4 and Uncoated/Fe_3O_4 samples show the highest temperature change of $\Delta T = 44$ °C and 51 °C respectively after 35 min of magnetic field exposure, while PS/Fe3O4 and Si/PS/Fe_3O_4 exhibit much lower temperature change of $\Delta T = 14$ °C and 18 °C respectively.

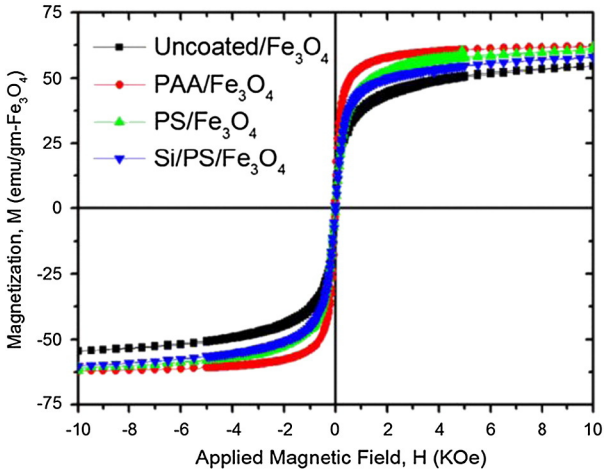

Fig. 8. DC magnetization curve scaled for per gram of Fe_3O_4 nanoparticles.

The different magnetic hyperthermia heating behaviors from these nanoparticle systems can be explained by the characteristics of the nanoparticles. Each nanoparticle system is structured differently in terms of configuration, inter-particle spacing, and physical confinement, where all these quantities may significantly impact the heating performance of the nanoparticles. The characteristic heating ability of each nanoparticle systems can be approximated by calculating the specific absorption rate (SAR) which is represented by the equation [32]:

$$\mathrm{SAR} = C_{\mathrm{water}} \frac{m_s}{m_i} \left(\frac{dT}{dt}\right)_{initial}, \tag{7}$$

where C is the specific heat capacity of the sample. As the mass of the iron oxide content is small in the fluid, the specific heat capacity is assumed to be equal to that of water which is 4.18 $Jg^{-1}°C^{-1}$. m_s is the total mass of the sample, m_i is the mass of the iron oxide in the sample solution, and $\left(\frac{dT}{dt}\right)_{initial}$ is the initial slope. SAR is determined using the initial slope of the heating curve. Note that an adiabatic condition was maintained during the experiment for minimizing the initial heat loss. The initial slope is determined from the first 200 s of the heating graph where temperature rise with time is almost linear. Fig. 10(a) shows the initial heating rate as a function of concentration, which shows almost a linear trend. This heating rate was used to calculate the SAR of the magnetic nanoparticles at the concentrations investigated

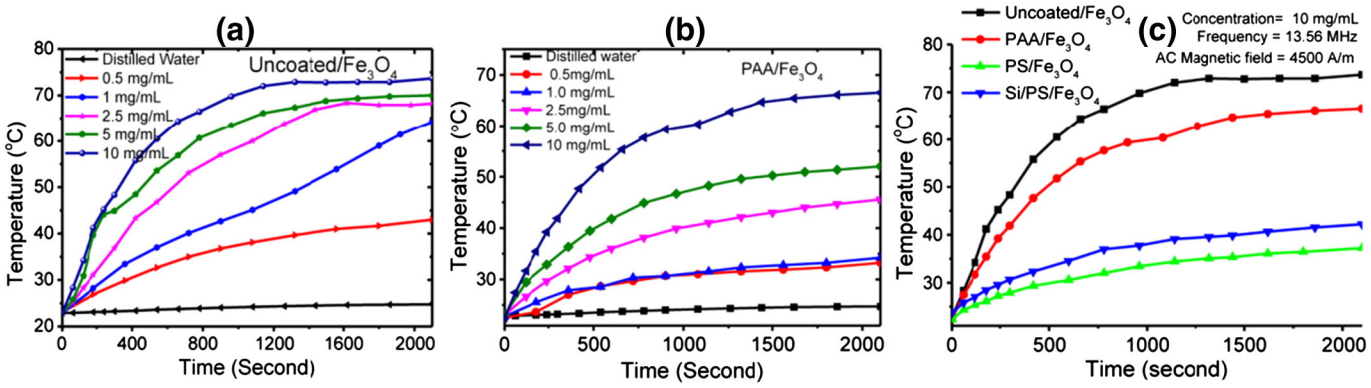

Fig. 9. Heating curve of (a) Uncoated/Fe_3O_4 (b) PAA/Fe_3O_4 at five different concentrations and (c) heating behavior of all four samples at a fixed concentration of 10 mg/mL.

[Fig. 10(b)]. The highest SAR value of 169 W/g was found for 0.5 mg/mL of Uncoated/Fe_3O_4, 110 W/g for PAA/Fe_3O_4 at the same concentration investigated. According to a report by Hergt et al. the magnetic nanoparticles having SAR of 100 W/g is a suitable choice for hyperthermia application [33].

The heat dissipation for an assembly of superparamagnetic particles arises due to the delay of the magnetic moment response in an AC magnetic field. Three potential mechanisms are responsible for nanoparticles heating in AC field, namely: Néel relaxation, Brownian relaxation, and hysteresis loss. In the case of Néel relaxation, heat dissipation occurs when particles overcome an energy barrier, $E_B = KV_{\sin^2}\theta$ (where, K is the effective magnetic anisotropy constant and $V = \frac{4}{3}\pi r^3$ is the particle volume with radius r, and θ is the angle between the magnetization and anisotropy axis), in an alternating magnetic field. At zero magnetic field, minimum energy of the particle occurs at $\theta = 0$ and $\theta = \pi$, which are the two equilibrium positions of the particle moment. However, as the temperature increases, thermal fluctuation k_BT (where k_B is the Boltzmann constant of $1.38 \times 10^{-23}{}^{J}/_{K}$ and T the absolute temperature) is large enough to overcome the anisotropy barrier E_B, which causes the magnetic moment of the particles to fluctuate rapidly in different anisotropic directions and resulting zero net magnetization is observed for an assembly of superparamagnetic particles. This behavior of the particle is more analogous to the paramagnetic particles and can be described by an effective paramagnetic model. For a superparamagnetic particle containing 10^5 atoms, it is described as a single-domain material and acting as a giant magnetic moment. The characteristic time related to the thermal fluctuation of magnetization with different anisotropy axis is given by Arhenius and first introduced by Néel in the following equation [5,34]:

$$\tau_N = \frac{\sqrt{\pi}}{2}\tau_o\left[\exp\left(\frac{KV}{k_BT}\right)\right]\Big/\left[\sqrt{{}^{KV}/_{k_BT}}\right], \tag{8}$$

where, τ_o is in the order of 10^{-9}–10^{-13} s.

In case of the Brownian relaxation, heating of the particles in liquid suspension occurs due to viscous drag between the particles and liquid, where the entire particle has a rotational movement with an applied AC magnetic field. The Brownian relaxation time is given by the following equation [5]:

$$\tau_B = \frac{3\eta V_H}{k_BT}, \tag{9}$$

where η is the viscosity of the liquid and V_H is the hydrodynamic volume of the particle.

Generally, both Néel and Brownian relaxations can occur at the same time. The relaxation of the particle is characterized by the effective relaxation time τ_{eff}, defined as: $\frac{1}{\tau_{eff}} = \frac{1}{\tau_B} + \frac{1}{\tau_N}$. The time delay between the alignment time defined, as the measurement time $\tau_{measurement} = \frac{1}{2\pi f}$, and the effective relaxation time, at a given frequency is responsible for dissipation of energy. If $\tau_{measurement} > \tau_{effective}$, then particle relaxes by dumping energy into the fluid and if $\tau_{measurement} < \tau_{effective}$, then no magnetic relaxation takes place as AC field is changing too fast. From the above equation it is clear that Néel relaxation can be influenced by

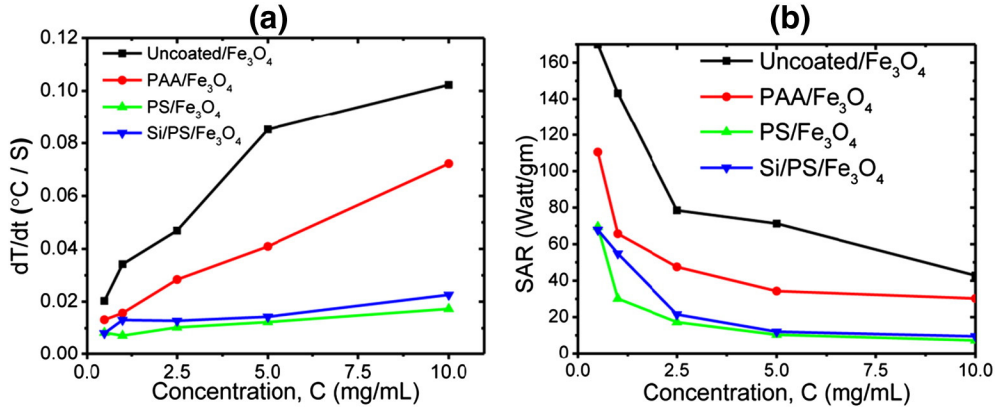

Fig. 10. (a) Initial heating rate of all samples at five different concentrations and (b) variation of SAR with respect to the nanoparticle concentrations.

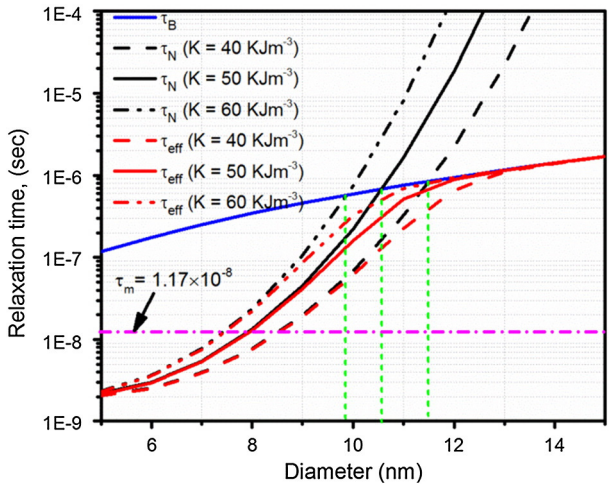

Fig. 11. Brownian, Néel and effective relaxation time as a function of particles diameter for different values of anisotropy constant (K).

changing the anisotropic properties and diameter of the particles, while Brownian relaxation can be adjusted by dispersing the nanoparticles in different viscous medium or particle size. Using $\eta = 0.888$ mPa-s (given by the zeta sizer), the expression for Néel, Brownian, and effective relaxations is demonstrated graphically as a function of particles diameter in Fig. 11 for different values of anisotropy constant (K), where the horizontal dashed line represents the measurement time (τ_m) and vertical dashed line represents the inflection point where both Brownian and Néel relaxation processes are equally contributing to the energy dissipation.

From Fig. 11 it is observed that, if $K = 40\ KJm^{-3}$, both Brownian and Néel relaxations contribute equally to hyperthermia heating for the particle diameter of 11.51 nm. As the particle size decreases to 11.51 nm, effective relaxation is dominated by the Néel relaxation process. For particle diameter greater than 11.51 nm, Brownian relaxation sets in. Thus, a critical diameter is defined at which both relaxation mechanisms are effective. It is found that, as the anisotropy constant increases to $50\ KJm^{-3}$, this critical diameter decreases to 10.56 nm. It is further reduced for even lower anisotropy constant. Thus, it is clear that the magnetic hyperthermia heating is strongly affected by the anisotropic properties and size of the particles. On the other hand, Vallejo-Fernandez et al. showed that above certain critical diameter in a very small field hysteresis losses dominant over the susceptibility loss [35]. This critical diameter is defined by:

$$D_p(0) = \left(\frac{6k_BT\ln(f\tau_o)}{\pi K}\right)^{1/3}, \tag{10}$$

where, τ_o is assumed to be 10^{-9} s, f is the frequency of the measurement (in this case, $f = 13.56$ MHz), and K is the anisotropy constant of the particles. Therefore using the experimentally determined anisotropy constant (K) of the particles for each sample (see Section 3.4), the critical diameters of the particles are found to be 6.84 nm, 8.46 nm, 7.29 nm and 6.98 nm for Uncoated/Fe_3O_4, PAA/Fe_3O_4, PS/Fe_3O_4 and Si/PS/Fe_3O_4 respectively. This analysis leads to conclusion that for a highly polydisperse sample all three mechanisms of heating can be effective.

Table 2
Brownian and Néel relaxation time of different nanoparticle systems.

Sample information	Brownian relaxation time τ_B(sec)	Néel relaxation time τ_N(sec)
Uncoated/Fe_3O_4	8.91×10^{-3}	8.82×10^{-9}
PAA/Fe_3O_4	1.34×10^{-5}	2.37×10^{-9}
PS/Fe_3O_4	4.18×10^{-3}	4.25×10^{-9}
Si/PS/Fe_3O_4	2.47×10^{-3}	2.2×10^{-9}

An attempt has been made to find qualitative information about different heating mechanisms involved in variety of systems. Using the results of DLS, volume weighted thickness from XRD and the effective anisotropy constant calculated from the DC magnetization data, both Brownian and Néel relaxation times of the fore-mentioned nanoparticle systems were calculated. Table 2 shows the Brownian and Néel relaxation times calculated for different nanoparticle systems using Eqs. (8)–(9). As can be seen from the table, Brownian relaxation time for each nanoparticle system is much higher than the measurement time of $\tau_{measurement} = 1.173 \times 10^{-8}$ s. Therefore, Brownian relaxation cannot be a dominant mechanism for heating of the particles in the alternating magnetic field at a frequency of 13.56 MHz. On the other hand, Néel relaxation time for each system of nanoparticle is of the order of 10^{-9} s, which is much faster than Brownian relaxation time and shorter than measurement time. It is then reasonable to conclude that Néel relaxation and hysteresis loss are the main mechanisms in the hyperthermia heating process at the frequency of 13. 56 MHz.

It has been found in several previous researches that intracellular magnetic heating is less efficient than heating of the particles in the aqueous solution due to reduction of Brownian motion in the cell [36]. Most of the intracellular heating mainly originated from the Néel relaxation mechanism. Considering Néel relaxation and hysteresis loss as the main mechanisms for hyperthermia heating, it has been evident that heating in presence of AC field is affected by several structural characteristics of the nanoparticles. These include the particle distribution, interparticle spacing, configuration, and confinement. Any changes in these material characteristics can alter magnetic relaxation process, and in turn affect hyperthermia heating behaviors. Therefore, to understand the heating mechanism of NPs in AC magnetic field, the effect of dipole–dipole interaction on hyperthermia heating behavior is taken into account. Furthermore, due to agglomeration of the particles, hysteresis heating can also be a dominant mechanism over Néel relaxation in AC magnetic field.

3.6. Relation between magnetic dipole interaction and hyperthermia heating

In this study, we propose a physical model in terms of dipolar interactions, which is illustrated in Fig. 12. The dipolar interaction energy between two particles with magnetic moments m_i and m_j at the position r_i ($i = 1$ and 2) and r_j are given by [37]:

$$E_{d-d} = \frac{\mu_o}{4\pi_{r_{ij}^3}}\left[\vec{m}_i\cdot\vec{m}_j - \frac{3}{r_{ij}^2}\left(\vec{m}_i\cdot\vec{r}_{ij}\right)\left(\vec{m}_j\cdot\vec{r}_{ij}\right)\right], \tag{11}$$

where $\vec{r}_{ij} = \vec{r}_i - \vec{r}_j$ is the separation distance between the two particles. If $m_1 = m_2 = m$ and the magnetic moments of the particles are in the same direction, that is along the direction of r_{12} the above equation is simplified to

$$E_{d-d} = \frac{-2\mu_o m^2}{4\pi_{r_{12}^3}}. \tag{12}$$

If the magnetic moments of the particles are in the perpendicular directions of r_{12}, this equation can be written as:

$$E_{d-d} = \frac{\mu_o m^2}{4\pi_{r_{12}^3}}. \tag{13}$$

From Eqs. (11)–(13), it is clear that the dipolar interaction energy increases as the interparticle separation decreases. In other words, the particles tend to agglomerate in the presence of strong dipole–dipole interactions.

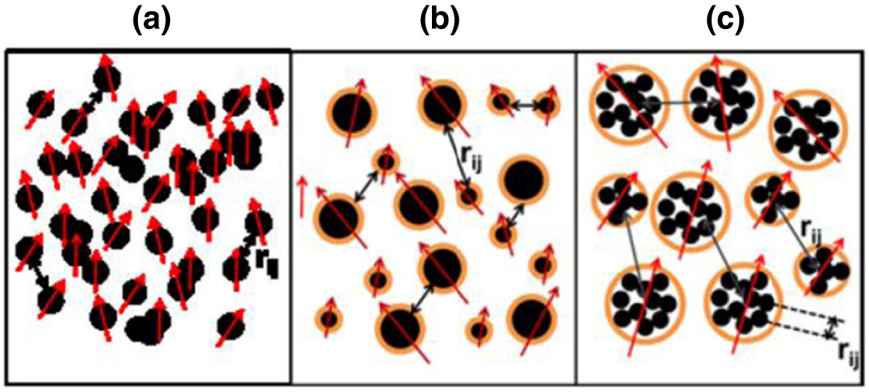

Fig. 12. Schematic diagram of the different nanoparticle system (a) representative of uncoated nanoparticles (b) nanoparticles coated with polymer (c) nanoparticles embedded in nanosphere matrix.

Due to dipole interaction, the moment of the particle coupled antiferromagnetically can be compared to a unidirectional anisotropy of each nanoparticle [37]. But this unidirectional anisotropy does not affect the low field magnetization or Néel relaxation if easy directions of all nanoparticles are uniformly distributed in all directions [38], which agrees well with our explanation described in Section 3.4. In fact, this antiferromagnetic coupling is likely the origin of hysteresis loss at highest concentrations for all nanoparticle systems investigated.

According to the model presented in Fig. 12, single Uncoated/Fe_3O_4 nanoparticles can relax either by switching their magnetic moment in response to AC field or by the physical rotation of the particle itself. However, for $\tau_{measurement} \ll \tau_B$, we can easily neglect the relaxation by Brownian motion. Moreover, TEM and DLS results show that Uncoated/Fe_3O_4 has considerable agglomeration, which apparently increases the effective particle size. Therefore, in addition to Néel relaxation, hysteresis loss may also be possible for larger clusters. This idea is further supported by experimental evidence, where a small hysteresis loop is observed in the DC magnetization curve of Uncoated/Fe_3O_4, as shown in the inset of Fig. 6(a) at higher concentrations. On the other hand, the strength of dipolar interaction in PAA/Fe_3O_4 is assumed to be much smaller due to surface coating. However, as the concentration increases, a minor hysteresis loop also appears for the PAA/Fe_3O_4 sample at the highest concentration of 10 mg/mL [inset of Fig. 6(b)]. Then, by integrating the area of the magnetization curve, the hysteresis loop area can be calculated. The loss due to hysteresis heating is just the area of the loop multiplied by applied AC frequency. The integration gives a value of the loop area to be 1.72 (a.u) for Uncoated/Fe_3O_4 while it is 10.63 (a.u) for PAA/Fe_3O_4 at the same concentration. These results suggest that most of the heating in PAA/Fe_3O_4 arises due to hysteresis loss, while heating in Uncoated/Fe_3O_4 may be dominant by the susceptibility loss and magnetic stirring. A recent report by Vallejjo-Fernandez et al. showed that the contribution in overall heating by Néel relaxation process is negligible while hysteresis heating and heating due to magnetic stirring can be the dominant mechanism over certain critical diameter (~13 nm) of Fe_3O_4 nanoparticles that were exposed to 111.5 KHz alternating magnetic field [35]. The critical diameter found in this study is 6.84 nm for Uncoated/Fe_3O_4 and 8.46 nm for PAA/Fe_3O_4. For a 9 nm average diameter of Uncoated/Fe_3O_4, it can be concluded that most of the heating in this sample arises from the hysteresis loss and stirring effect, which is consistent with our previous hypothesis. Consequently, much higher heating is observed for Uncoated/Fe_3O_4 compared to PAA/Fe_3O_4. For PS/Fe_3O_4 and Si/PS/Fe_3O_4, the Fe_3O_4 nanoparticles are embedded and physically confined in the polystyrene matrix. In this situation, the interparticle separation is small which is on the order of one particle diameter. Thus, it is difficult to thermally activate this system at a low AC field, where the nanoparticles have to overcome the dipolar field produced by discrete nanoparticles. Therefore, only hysteresis loss may be responsible for self-heating in these nanoparticle assemblies. As a result, a much reduced hyperthermia output was observed from both PS/Fe_3O_4 and Si/PS/Fe_3O_4. A minor hysteresis loop is shown in the inset of Fig. 6(a–d) at higher concentrations indicating the contributions from the hysteresis loss. The areas of the hysteresis loop calculated for PS/Fe_3O_4 and Si/PS/Fe_3O_4 are 4.95 (a.u) and 7.65 (a.u) respectively, which are smaller than that calculated for PAA/Fe_3O_4. Consequently, a much reduced hyperthermia output was detected from these samples.

The effect of the dipolar interaction on hyperthermia heating behavior of the MNP systems can be investigated by varying the interparticle distance i.e. at varying concentrations. Our experimental observation shows that the overall SAR of all nanoparticle samples decreases at higher concentrations [Fig. 10(b)]. This behavior can be explained by considering the co-occurrence of Néel relaxation and hysteresis mechanism for non-aggregated and aggregated nanoparticles, respectively. As the concentration increases, the particles tend to agglomerate (confirmed by measuring DLS) resulting in a larger dipolar interaction. Therefore, it is likely that Néel relaxation progressively decreases at higher concentrations and the hysteresis loss is the only dominant mechanism. Similar behavior was observed by Urtizberea et al. [39] and Piñeiro-Redondo et al. [40], where they attributed the decrease in SAR with increasing nanoparticle concentrations due to dipole interactions for single domain superparamagnetic nanoparticles. A recent study on ferrite-based nanoparticles by Luis C. Branquinho et al. shows that, as the particle concentration increases, chain formation is more favorable and resulting in decreases in SAR [41]. Their results show that, with the decreasing interparticle separation, the chain length increases which ultimately reduces the heating performance. Therefore, a theoretical model based on dipole–dipole interactions valid for low field regime is also proposed by the same authors. They concluded that the experimental conditions, optimal chain size and diameter of the particles all significantly affect the heating ability of the nanoparticles. On the other hand, according to Serantes et al., computational technique is effective in finding the effect of interaction for an assembly of superparamagnetic particles. They developed a Monte Carlo (MC) method based on the metropolis algorithm and found that the higher heating of the single domain MNPs is associated with the decrease of hysteresis loss at high nanoparticle concentrations [14]. Based on these studies, it can be concluded that the dipole interaction is enhanced by having a shorter interparticle separation at a higher concentration. This will lead to a decrease in SAR.

3.7. Field dependence of SAR

In order to further investigate the dominant heating mechanism, the heating profiles are established for each nanoparticle system at different AC field amplitudes. Fig. 13(a–c) shows the time dependent heating curves of 10 mg/mL Uncoated/Fe_3O_4, PAA/Fe_3O_4 and PS/Fe_3O_4 at

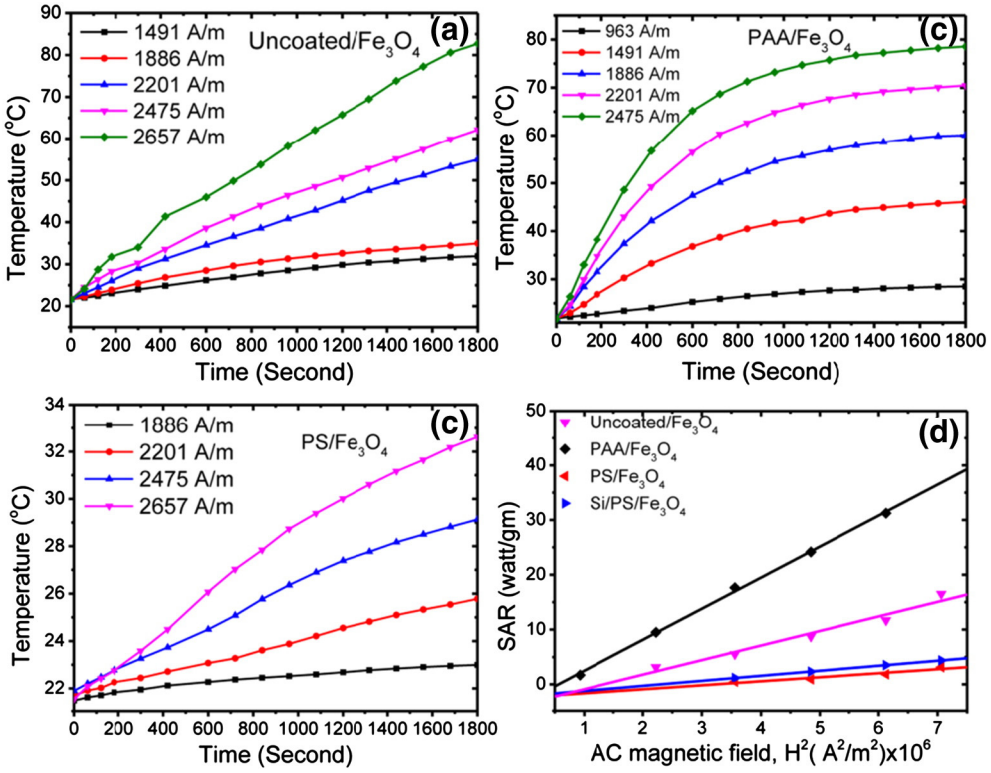

Fig. 13. Time dependent temperature curve at different AC magnetic field strength for (a) Uncoated/Fe_3O_4 (b) PAA/Fe_3O_4 and (c) PS/Fe_3O_4 and (d) variation of SAR with square of AC magnetic field strength.

different AC magnetic field amplitudes. Each curve shows a sharp increase in temperature as the magnetic field increases. According to the linear response theory (LRT), SAR shows square field dependence which can be expressed by the following equation [32]:

$$SAR = \frac{\mu_o H^2 2\pi^2 f^2 \chi_o \tau_{eff}}{1 + \left(2\pi f \tau_{eff}\right)^2}. \quad (14)$$

Fig. 13(d) shows SAR as a function of square of the AC field, that has a linear trend with increasing field. This result is in good agreement with the theoretical model as predicted by Rosenweig and also experimentally verified by Xuman Wang et al. [42].

4. Conclusion

In this work, magnetic hyperthermia behaviors of different Fe_3O_4 nanoparticles systems (confined and unconfined) were investigated in high frequency alternating field. The experimental results of DC magnetization measurements show superparamagnetic characteristics of all Fe_3O_4 samples at room temperature. The experimental results on the different nanoparticle systems show a clear correlation between magnetic hyperthermia heating and dominating structural factors including physical arrangement, size, and anisotropy. The confined systems (PS/Fe_3O_4 and Si/PS/Fe_3O_4) are nanoscale Fe_3O_4 (10 nm) particles embedded in the matrix of polystyrene spheres (100 nm). The unconfined ones are free Fe_3O_4 nanoparticles of similar dimensions well dispersed in liquid (Uncoated/Fe_3O_4, PAA/Fe_3O_4). Their heating curves were analyzed by taking into account of the Néel and Brownian relaxations, hysteresis loss, and magnetic dipole–dipole interactions.

Based on our analysis we are able to conclude that: (1) specific absorption rates (SAR) of the unconfined NP systems (such as Uncoated/Fe_3O_4, PAA/Fe_3O_4) are higher than the confined ones (PS/Fe_3O_4 and Si/PS/Fe_3O_4); (2) the increased SAR values in the unconfined NP systems are attributed to Néel relaxation and hysteresis loss, and (3) the confined systems exhibit lower SAR values due to dipole–dipole interactions. A physical model was proposed to explain the effect of dipole interactions on the hyperthermia heating behavior of the Fe_3O_4 nanoparticles.

Acknowledgments

Work at the Ames Laboratory was supported by the Department of Energy, Basic Energy Sciences, Division of Materials Sciences and Engineering under Contract No. DE-AC02-07CH11358. The work at Tongji University was supported by grants from Shanghai Nanotechnology Promotion Center (grant No. 11 nm0506100, 12nm0501201) and the National Natural Science Foundation of China (51173135). Research at the University of Cincinnati was partially supported by a grant from the National Science Foundation under contract No. EEC-1343568. The authors would like to thank Dr. Barry Maynard, Professor, Department of Geology, University of Cincinnati for the X-ray diffraction of the analyzed samples.

References

[1] A. Jordan, R. Scholz, P. Wust, H. Fähling, R. Felix, Magnetic fluid hyperthermia (MFH): cancer treatment with AC magnetic field induced excitation of biocompatible superparamagnetic nanoparticles, J. Magn. Magn. Mater. 201 (1999) 413–419.
[2] Q.A. Pankhurst, J. Connolly, S.K. Jones, J. Dobson, Applications of magnetic nanoparticles in biomedicine, J. Phys. D. Appl. Phys. 36 (2003) R167.
[3] A.P. Khandhar, R.M. Ferguson, K.M. Krishnan, Monodispersed magnetite nanoparticles optimized for magnetic fluid hyperthermia: implications in biological systems, J. Appl. Phys. 109 (2011) 07B310-3.
[4] C. Martinez-Boubeta, K. Simeonidis, A. Makridis, M. Angelakeris, O. Iglesias, P. Guardia, A. Cabot, L. Yedra, S. Estrade, F. Peiro, Z. Saghi, P.A. Midgley, I. Conde-Leboran, D. Serantes, D. Baldomir, Learning from nature to improve the heat generation of iron-oxide nanoparticles for magnetic hyperthermia applications, Sci. Rep. 3 (2013).
[5] R.E. Rosensweig, Heating magnetic fluid with alternating magnetic field, J. Magn. Magn. Mater. 252 (2002) 370–374.
[6] R. Hergt, R. Hiergeist, M. Zeisberger, D. Schüler, U. Heyen, I. Hilger, W.A. Kaiser, Magnetic properties of bacterial magnetosomes as potential diagnostic and therapeutic tools, J. Magn. Magn. Mater. 293 (2005) 80–86.

[7] R. Hergt, S. Dutz, R. Müller, M. Zeisberger, Magnetic particle hyperthermia: nanoparticle magnetism and materials development for cancer therapy, J. Phys. Condens. Matter 18 (2006) S2919.
[8] B. Mehdaoui, A. Meffre, J. Carrey, S. Lachaize, L. Lacroix, M. Gougeon, B. Chaudret, M. Respaud, Optimal size of nanoparticles for magnetic hyperthermia: a combined theoretical and experimental study, Adv. Funct. Mater. 21 (2011) 4573–4581.
[9] A. Meffre, B. Mehdaoui, V. Kelsen, P.F. Fazzini, J. Carrey, S. Lachaize, M. Respaud, B. Chaudret, A simple chemical route toward monodisperse iron carbide nanoparticles displaying tunable magnetic and unprecedented hyperthermia properties, Nano Lett. 12 (2012) 4722–4728.
[10] C.H. Li, P. Hodgins, G.P. Peterson, Experimental study of fundamental mechanisms in inductive heating of ferromagnetic nanoparticles suspension (Fe_3O_4 iron oxide ferrofluid), J. Appl. Phys. 110 (2011) 054303–054310.
[11] C.J. Bae, S. Angappane, J.-G. Park, Y. Lee, J. Lee, K. An, T. Hyeon, Experimental studies of strong dipolar interparticle interaction in monodisperse Fe_3O_4 nanoparticles, Appl. Phys. Lett. 91 (2007) 102502–102503.
[12] C. Haase, U. Nowak, Role of dipole–dipole interactions for hyperthermia heating of magnetic nanoparticle ensembles, Phys. Rev. B 85 (2012) 045435.
[13] V. Singh, V. Banerjee, Ferromagnetism, hysteresis and enhanced heat dissipation in assemblies of superparamagnetic nanoparticles, J. Appl. Phys. 112 (2012) 114912–114918.
[14] D. Serantes, D. Baldomir, C. Martinez-Boubeta, K. Simeonidis, M. Angelakeris, E. Natividad, M. Castro, A. Mediano, D.-X. Chen, A. Sanchez, L. Balcells, B. Martinez, Influence of dipolar interactions on hyperthermia properties of ferromagnetic particles, J. Appl. Phys. 108 (2010) 073918-5.
[15] F. Xu, C. Cheng, D. Chen, H. Gu, Magnetite nanocrystal clusters with ultra-high sensitivity in magnetic resonance imaging, ChemPhysChem 13 (2012) 336–341.
[16] R. Molday, Patent 4,452,773, 1984, U.S. Patent 1984;4,452,773.
[17] H. Xu, L. Cui, N. Tong, H. Gu, Development of high magnetization Fe_3O_4/polystyrene/silica nanospheres via combined miniemulsion/emulsion polymerization, J. Am. Chem. Soc. 128 (2006) 15582–15583.
[18] J. Sun, S. Zhou, P. Hou, Y. Yang, J. Weng, X. Li, M. Li, Synthesis and characterization of biocompatible Fe_3O_4 nanoparticles, J. Biomed. Mater. Res. A 80A (2007) 333–341.
[19] P. Arkai, R.J. Merriman, B. Roberts, D.R. Peacor, M. Toth, Crystallinity, crystallite size and lattice strain of illite–muscovite and chlorite: comparison of XRD and TEM data for diagenetic to epizonal pelites, Eur. J. Mineral. 8 (1996) 1119–1137.
[20] V. Drits, J. Srodon, D. Eberl, XRD measurement of mean crystallite thickness of illite and illite/smectite: reappraisal of the Kubler index and the Scherrer equation, Clays Clay Miner. 45 (1997) 461–475.
[21] D. Eberl, R. Nüesch, V. Sucha, S. Tsipursky, Measurement of fundamental illite particle thicknesses by X-ray diffraction using PVP-10 intercalation, Clays Clay Miner. 46 (1998) 89–97.
[22] D.D. Eberl, V. Drits, J. Srodon, R. Nüesch, MudMaster: a program for calculating crystallite size distributions and strain from the shapes of X-ray diffraction peaks, US Geological Survey Open File Report, 961996. 44.
[23] D.D. Eberl, J. Srodon, V.A. Drits, Comment on“ Evaluation of X-ray diffraction methods for determining the crystal growth mechanisms of clay minerals in mudstones, shales and slates,” by LN Warr and DR Peacor, Swiss Bull. Mineral. Petrol. 83 (2003) 349–358.
[24] J. Dormann, D. Fiorani, E. Tronc, Magnetic relaxation in fine-particle systems, Adv. Chem. Phys. 98 (1997) 283–494.
[25] A.A. Allam, M.E. Sadat, S.J. Potter, D.B. Mast, D.F. Mohamed, F.S. Habib, G.M. Pauletti, Stability and magnetically induced heating behavior of lipid-coated Fe_3O_4 nanoparticles, Nanoscale Res. Lett. 8 (2013) 1–7.
[26] M. Shliomis, Magnetic fluids, Sov. Phys. Uspekhi 17 (1974) 153.
[27] S. Laurent, S. Dutz, U.O. Häfeli, M. Mahmoudi, Magnetic fluid hyperthermia: focus on superparamagnetic iron oxide nanoparticles, Adv. Colloid Interface Sci. 166 (2011) 8–23.
[28] E.C. Stoner, E. Wohlfarth, A mechanism of magnetic hysteresis in heterogeneous alloys, Philos. Trans. R. Soc. Lond. A Math. Phys. Sci. (1948) 599–642.
[29] M. Respaud, Magnetization process of noninteracting ferromagnetic cobalt nanoparticles in the superparamagnetic regime: deviation from Langevin law, J. Appl. Phys. 86 (1999) 556–561.
[30] J. Carrey, B. Mehdaoui, M. Respaud, Simple models for dynamic hysteresis loop calculations of magnetic single-domain nanoparticles: application to magnetic hyperthermia optimization, J. Appl. Phys. 109 (2011) (083921-083921-17).
[31] W.F. Brown, Theory of the approach to magnetic saturation, Phys. Rev. 58 (1940) 736–743.
[32] M. Gonzales-Weimuller, M. Zeisberger, K.M. Krishnan, Size-dependant heating rates of iron oxide nanoparticles for magnetic fluid hyperthermia, J. Magn. Magn. Mater. 321 (2009) 1947–1950.
[33] R. Hergt, S. Dutz, Magnetic particle hyperthermia-biophysical limitations of a visionary tumour therapy, J. Magn. Magn. Mater. 311 (2007) 187–192.
[34] L. Néel, Some theoretical aspects of rock-magnetism, Adv. Phys. 4 (1955) 191–243.
[35] G. Vallejo-Fernandez, O. Whear, A. Roca, S. Hussain, J. Timmis, V. Patel, K. O'Grady, Mechanisms of hyperthermia in magnetic nanoparticles, J. Phys. D 46 (2013) 312001.
[36] J. Fortin, F. Gazeau, C. Wilhelm, Intracellular heating of living cells through Néel relaxation of magnetic nanoparticles, Eur. Biophys. J. 37 (2008) 223–228.
[37] D. Chen, A. Sanchez, H. Xu, H. Gu, D. Shi, Size-independent residual magnetic moments of colloidal Fe_3O_4-polystyrene nanospheres detected by ac susceptibility measurements, J. Appl. Phys. 104 (2008) 093902.
[38] C. Bean, J. Livingston, Superparamagnetism, J. Appl. Phys. 30 (1959) S120–S129.
[39] A. Urtizberea, E. Natividad, A. Arizaga, M. Castro, A. Mediano, Specific absorption rates and magnetic properties of ferrofluids with interaction effects at low concentrations, J. Phys. Chem. C 114 (2010) 4916–4922.
[40] Y. Piñeiro-Redondo, M. Bañobre-López, I. Pardiñas-Blanco, G. Goya, M.A. López-Quintela, J. Rivas, The influence of colloidal parameters on the specific power absorption of PAA-coated magnetite nanoparticles, Nanoscale Res. Lett. 6 (2011) 1–7.
[41] L.C. Branquinho, M.S. Carrião, A.S. Costa, N. Zufelato, M.H. Sousa, R. Miotto, R. Ivkov, A.F. Bakuzis, Effect of magnetic dipolar interactions on nanoparticle heating efficiency: implications for cancer hyperthermia, Sci. Rep. 3 (2013).
[42] X. Wang, H. Gu, Z. Yang, The heating effect of magnetic fluids in an alternating magnetic field, J. Magn. Magn. Mater. 293 (2005) 334–340.